Tensor Networks and Geometry for the Modelling of Disordered Quantum Many-Body Systems

Andrew M. Goldsborough[1, 2, *] and Rudolf A. Römer[2, †]

[1]*Max Planck Institute for Quantum Optics,*
Hans-Kopfermannstr. 1, D-85748 Garching, Germany
[2]*Department of Physics and Centre for Scientific Computing,*
The University of Warwick, Coventry, CV4 7AL, United Kingdom
(Dated: August 9, 2016)

I. INTRODUCTION

At its most fundamental level a quantum many-body system can be defined by a Hilbert space $\mathcal{H}$ and a Hamiltonian H describing the evolution of states in $\mathcal{H}$. But with $\sim 2^{10^{23}}$ states for just a single mole of, e.g., spin-1/2 particles, computing ground states and excitations remains a formidable challenge. Fortunately, advanced numerical methods have been developed in the last decades to tackle the problem. Whilst density-functional theory, dynamical mean-field theory, quantum Monte Carlo and their variants and extensions have allowed us to study systems with hundreds – and sometimes thousands – of atoms in three dimensions, large strongly correlated systems are more problematic. However, much has been learned in low dimensional systems by applying concepts from quantum information to many body physics. At the heart of this understanding lies the realization that not all states in $\mathcal{H}$ are equal in terms of their entanglement properties. For a general state in $\mathcal{H}$ the entanglement entropy $S_{A|B}$ scales as the *volume* of subsystem. However, for ground states of *gapped* systems, the entanglement scales as the *area* of the boundary separating the subsystems. This is the famous *area law* for entanglement entropy [1–3]. It suggests that much of the low energy physics is likely to be well described by a much smaller, area law satisfying subset of $\mathcal{H}$. The success of tensor network methods is down to their ability to capture the entanglement described by the area law and provide a variational ansatz within the space of area law satisfying states [4]. The simplest tensor network, the matrix product state (MPS), is at the heart of the density matrix renormalisation group (DMRG) algorithm, accepted to be the most accurate approach for the numerical study of strongly correlated 1D systems [5]. In 2D, one has to use more sophisticated tensor networks such as projected entangled pair states (PEPS) to make progress.

The area law for $S_{A|B}$ in quantum-many body systems was foreshadowed in the theory of black hole thermodynamics. It had been found [6, 7] that black holes have a thermal Bekenstein-Hawking entropy $S_{BH} = \frac{\mathcal{A}_h}{4G}$, that scales with the surface area $\mathcal{A}_h$ of the black hole horizon; G is Newton's gravitational constant. For $S_{A|B}$, Ryu and Takayanagi [8] suggest a similar extension in the context of the so-called AdS/CFT correspondence, i.e. the duality between quantum gravity on a $D+2$ dimensional Anti-de Sitter (AdS) spacetime and a conformal field theory (CFT) defined on its $D + 1$ dimensional boundary [9]. The entanglement entropy of a region A of the CFT is related to the size of the surface with smallest area, or *minimal surface γ_A*, within the AdS bulk that separates A from the rest of the system. This is shown pictorially in fig. 1. In condensed matter systems, AdS/CFT can provide a geometric interpretation of the renormalization group (RG) approach. The additional *holographic* dimension can be interpreted as a scale factor in the RG coarse graining [10]. This analogy gives $S_{A|B} = \frac{\mathcal{A}_{\gamma_A}}{4G_N^{(D+2)}}$, where $\mathcal{A}_{\gamma_A}$ is the area of the minimal

---

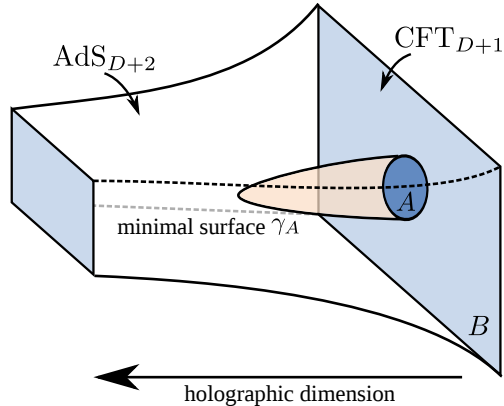[*] andrew.goldsborough@mpq.mpg.de
[†] r.roemer@warwick.ac.uk

FIG. 1. A diagrammatic representation of the AdS/CFT correspondence, showing a $(D+1)$ dimensional CFT on the boundary of a $(D+2)$ dimensional AdS spacetime. The entanglement entropy of a region A of the CFT is proportional to the minimal surface γ_A that separates A from the remainder of the CFT.

surface γ_A and $G_N^{(D+2)}$ is Newton's constant in $D+2$ dimensions. As we shall see, these concepts underpin the success of tensor networks that satisfy the area law and beyond.

For disordered *and* interacting systems, the variational refinement of tensor networks can already be too costly and has to be balanced with the need to additionally average of many, sometimes thousands of disorder realizations. As we will show here, instead of variationally refining a particular tensor network, a strategy that self-assembles the tensors according to a physically motivated, realisation-specific disordered network provides a viable alternative strategy.

II. MATRIX PRODUCT STATES

Consider a quantum system with basis states $|\uparrow\rangle$ and $|\downarrow\rangle$ for each site in a system with L sites. Simple *product states* can be formed as tensor product of the bases [11], for example $|\uparrow\rangle \otimes \cdots \otimes |\uparrow\rangle$. For, e.g. $L = 2$, any state can be written as a superposition of all possible two site product states,

$$|\Psi\rangle = (u_1 |\uparrow\rangle + d_1 |\downarrow\rangle) \otimes (u_2 |\uparrow\rangle + d_2 |\downarrow\rangle) = \sum_{\sigma_1,\sigma_2} C_{\sigma_1,\sigma_2} |\sigma_1\rangle \otimes |\sigma_2\rangle, \tag{1}$$

where σ_i can be $\uparrow$ or $\downarrow$, u_i, d_i are numerical coefficients and C_{σ_1,σ_2} is a two component tensor with elements

$$\mathbf{C} = \begin{pmatrix} u_1 u_2 & u_1 d_2 \\ d_1 u_2 & d_1 d_2 \end{pmatrix}. \tag{2}$$

Product states such as (1) have bases independent of each other and the expectation values factorise. On the other hand, *entangled* states such as

$$|\Psi\rangle = \frac{1}{\sqrt{2}} (|\uparrow\rangle \otimes |\downarrow\rangle - |\downarrow\rangle \otimes |\uparrow\rangle) \tag{3}$$

do not have factorising expectation values. The maximally entangled state (3) would require a tensor of the form

$$\mathbf{C} \equiv \begin{array}{c|cc} & \sigma_2 = \uparrow & \sigma_2 = \downarrow \\ \hline \sigma_1 = \uparrow & 0 & 1/\sqrt{2} \\ \sigma_1 = \downarrow & -1/\sqrt{2} & 0 \end{array} = \frac{1}{\sqrt{2}} \begin{pmatrix} 0 & 1 \\ -1 & 0 \end{pmatrix}, \tag{4}$$
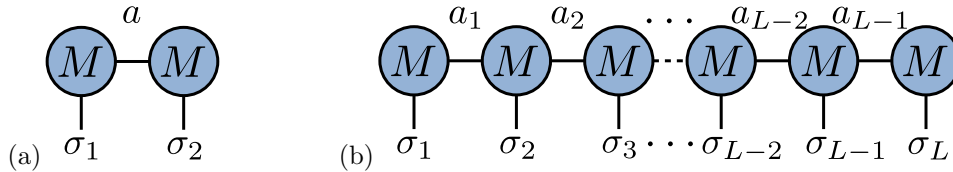
FIG. 2. Diagrammatic representation of (a) the two site MPS in eq. (6) and (b) the general L site MPS of eq. (7). The circles represent the M tensors and the lines are the tensor indices. The horizontal lines represent the bond indices, the vertical lines the physical indices.

which cannot be described by the coefficients u_1, d_1, u_2 and d_2 in eq. (2). Instead, let us introduce matrices [12],

$$\mathbf{M}_1 = \frac{1}{\sqrt[4]{2}}\begin{pmatrix} 1 & 0 \\ 0 & 1 \end{pmatrix} \quad , \quad \mathbf{M}_2 = \frac{1}{\sqrt[4]{2}}\begin{pmatrix} 0 & 1 \\ -1 & 0 \end{pmatrix}. \tag{5}$$

These matrices, combined using a standard matrix product, can easily produce the entangled state

$$C_{\sigma_1,\sigma_2} = \sum_a [\mathbf{M}_1]_a^{\sigma_1}\,[\mathbf{M}_2]_a^{\sigma_2} \quad \Rightarrow \quad \mathbf{C} = \frac{1}{\sqrt{2}}\begin{pmatrix} 0 & 1 \\ -1 & 0 \end{pmatrix}, \tag{6}$$

as desired. The a index introduces entanglement between the two states and can be thought of as a form of *bond*. Note that we have chosen the upper and lower placement of the indices for later convenience. Eq. (6) defines the simplest *matrix product state* (MPS). It can be expressed diagrammatically as in fig. 2(a), where the matrix is drawn as a circle and each index is represented by a line or *leg*. The matrix multiplication, or more generally tensor contraction, is shown by joining the lines that represent the summed over index. These diagrammatic representations of the state become very convenient for larger and more complicated tensor networks and are commonplace in the literature.

A general wavefunction on a lattice of L sites can be written as $|\Psi\rangle = \sum_{\sigma_1,\dots,\sigma_L} C_{\sigma_1\dots\sigma_L}\,|\sigma_1\rangle \otimes \cdots \otimes |\sigma_L\rangle$. As with the two site case, the $C_{\sigma_1\dots\sigma_L}$ tensor can be split into a series of local tensors with connections to their neighbours that allow the inclusion of entanglement. When away from boundaries each site has two neighbours thus the tensors at each site have three indices; one for the site basis and one for each neighbour. In full the wavefunction takes the form

$$|\Psi\rangle = \sum_{\sigma_1,\dots,\sigma_L}\ \sum_{a_1,\dots,a_{L-1}} M_{a_1}^{\sigma_1} M_{a_1 a_2}^{\sigma_2}\dots M_{a_{L-2}a_{L-1}}^{\sigma_L} M_{a_{L-1}}^{\sigma_L}\,|\sigma_1,\dots,\sigma_L\rangle, \tag{7}$$

where $|\sigma_1\dots\sigma_L\rangle \equiv |\sigma_1\rangle \otimes \cdots \otimes |\sigma_L\rangle$ and $M_{a_{i-1}a_i}^{\sigma_i} \equiv [\mathbf{M}_i]_{a_{i-1}a_i}^{\sigma_i}$. The σ_i indices label the spins of the basis and are known as the *physical indices*, whereas the a_i are the *bond*, *virtual* or *auxiliary indices*. To draw a distinction between the two index types, it is convention to have the physical σ_i as upper indices, thus giving the standard form of an MPS [5]. As before, the MPS can be represented diagrammatically as a chain of circles connected horizontally by the bond indices and with the physical indices drawn vertically as in fig. 2(b). Note that (7) corresponds to a state with open boundary conditions (OBCs) as is evident from the special tensors $M_{a_1}^{\sigma_1}$ and $M_{a_{L-1}}^{\sigma_L}$ at the sites 1 and L.

The MPS (7) is an exact representation of any state in $\mathcal{H}$. When increasing site index i up to the centre of the chain, the size of each $M_{a_{i-1}a_i}^{\sigma_i}$ increases. For example when $i = L/2$ the dimensions of the MPS tensor are $[d, d^{\frac{L}{2}-1}, d^{\frac{L}{2}}]$, where d is the dimension of the site basis, e.g. $d = 2$ for spin-1/2 systems. This means that the number of elements of the centre tensor is d^L as
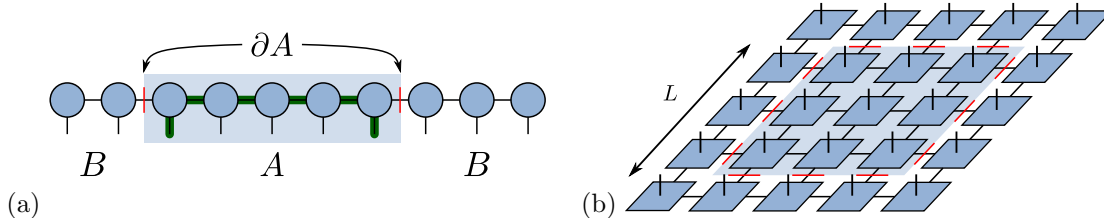
FIG. 3. (a) For an MPS a region A (shaded blue) is bounded by two bonds, denoted by red lines. If the size of A is increased the number of bonds stays at 2. The bold green line highlights the minimum path between two sites. (b) A PEPS on a square lattice, where the PEPS tensors are blue squares, the virtual indices are in the plane, and the physical indices are those pointing up. As before, the region under consideration is highlighted in blue and the bonds that separate it from the rest of the system are shown by red lines. Here the boundary scales as $4L$ and is therefore area law conserving.

expected when all of the information is preserved. By limiting the size of the bond indices, known as setting the *bond dimension* χ, one truncates the size of the Hilbert space allowing much larger system sizes to be computationally tractable. Setting χ also controls the amount of entanglement that the wavefunction (7) can have. Due to the fact that ground states of gapped Hamiltonians satisfy the area law, and therefore have relatively little entanglement, setting a finite χ still allows for an accurate description of the wavefunction. For example, while exact diagonalisation is usually limited to $L \sim 30$ sites [13], the MPS approach can study many hundreds of sites with $\chi \sim \mathcal{O}(10^3)$ [14]. The MPS can be used as a variational ansatz by *sweeping* back and forth across the chain choosing the contents of each $M^{\sigma_i}_{a_{i-1}a_i}$ that minimises the energy. This variational MPS algorithm is often referred to as DMRG, despite the fact that the original DMRG algorithm [15] does not use an MPS. A full discussion of MPS based DMRG can be found in reference [5].

III. TENSOR NETWORKS

A. The Area Law for Entanglement Entropy

As highlighted in the introduction, the area law states that the entanglement entropy for ground states in gapped quantum many body systems scales with the boundary of a subsystem rather than the volume. This means that these ground states are significantly easier to simulate on a classical computer than generic states. For tensor networks the *boundary* is quantified by the number of bonds n_A connecting region A to the environment B. The reasoning behind this measure is that if all of the tensors are identical, with a bond dimension χ the maximum contribution to the entanglement entropy per bond is $\log_2(\chi)$. Evenbly and Vidal [16] go further to suggest that for most cases of homogeneous tensor networks the entanglement per bond is approximately 1, hence $S_{A|B} \approx n_A$. The boundary of a region in a 1D system is simply two points and does not increase when the region is expanded. An MPS has these same properties; the number of bonds that one would have to cut to separate region A from B is 2 and does not change if the size of A is altered, as shown in fig. 3(a). The fact that the MPS has the same entanglement properties as the ground state of a gapped 1D system makes it an ideal variational ansatz for such problems and gives a reason for the excellent scaling for these systems.

The area law also explains why performance of DMRG for critical and 2D systems is worse. For critical systems the entanglement entropy scales logarithmically with the region size, $S_{A|B} \propto \log(L)$ [17, 18], hence the χ required for accurate DMRG increases with system size. For 2D, take for example a square lattice with a square region within it. If the region has side length L, the area law suggests that the entanglement entropy should scale as its boundary $S_{A|B} = 4L \propto L$, thus the

MPS is insufficient as a variational ansatz for this system. An area law conserving ansatz would be a tensor network where all sites are connected to their four neighbours to match the lattice geometry, as shown in fig. 3(b). This tensor network is known as a *projected entangled pair state* (PEPS) and is can be viewed as natural 2D extension of the MPS [19, 20].

B. Beyond the Area Law

Tensor networks, particularly the multi-scale entanglement renormalisation ansatz (MERA) [21, 22], can be seen as a coarse grained embodiment of AdS/CFT [16, 23]. The structure of MERA, shown in fig. 4(a), is made up of *disentanglers* (green squares) and *isometries* (pink triangles). The intuitive argument behind its construction is that the disentanglers remove short range entanglement so that the isometries can then remove degrees of freedom that are no longer coupled to the system. The network is self-similar in the way that at each level of coarse graining the network looks the same. This direction of coarse graining, perpendicular to the physical lattice, is the extra *holographic* dimension.

Just as with MPS and PEPS, the minimal surface γ_A is found by counting the minimum number of bonds that have to be cut to separate one region from the rest of the system. Take, for example, a region comprised of L sites within a MERA as shown in fig. 4(a). The minimum number of bonds (red lines in fig. 4(a)) $n_A \approx \log(L)$, which matches the entanglement scaling of critical systems [16]. As an extension of this, it was shown [24, 25] that in the continuum limit of MERA it has a metric that matches the properties of AdS/CFT.

In addition to entanglement entropy, similar arguments hold for two-point correlation functions [16, 23]. The asymptotic scaling of correlation functions should be

$$C_{\text{TN}}(x_1, x_2) \sim e^{-\alpha D_{\text{TN}}(x_1, x_2)}, \tag{8}$$

where D_{TN} is the path with the minimum distance or *geodesic* connecting points x_1 and x_2 within the tensor network. For MPS $D_{\text{MPS}} = |x_2 - x_1|$, as shown as the bold line in fig. 3(a). Hence

$$C_{\text{MPS}}(x_1, x_2) \sim e^{-\alpha D_{\text{MPS}}(x_1, x_2)} = e^{-|x_2 - x_1|/\xi}, \tag{9}$$

where ξ is the correlation length. MERA, on the other hand has path lengths that scale logarithmically with separation of x_1 and x_2 ($D_{\text{MERA}}(x_1, x_2) \propto \log_2(L)$), as shown in fig. 4(a). Thus

$$C_{\text{MERA}}(x_1, x_2) \sim e^{-\alpha D_{\text{MERA}}(x_1, x_2)} = |x_2 - x_1|^{-q}, \tag{10}$$

recovering the power law decay profile characteristic of critical systems.

IV. STRUCTURALLY INHOMOGENEOUS TENSOR NETWORKS

For *disordered* quantum many-body systems, the strong-disorder renormalisation group (SDRG) provides a powerful means of analysing a system by concentrating principally on the disorder within it. The approach was originally devised by Ma, Dasgupta and Hu [27, 28] for the random anti-ferromagnetic (AFM) Heisenberg chain where the coupling constant is different for each position, taking a random value. The principle behind the SDRG is to eliminate the most strongly coupled pairs of spins and replace them with an effective interaction that couples the spins at either side. The most strongly coupled pair are thought of as being *frozen* into a singlet ground state as the neighbouring interactions are significantly weaker – ultimately leading to the random singlet phase, which is the ground state of the system [29]. This freezing out of pairs of sites is conceptually similar
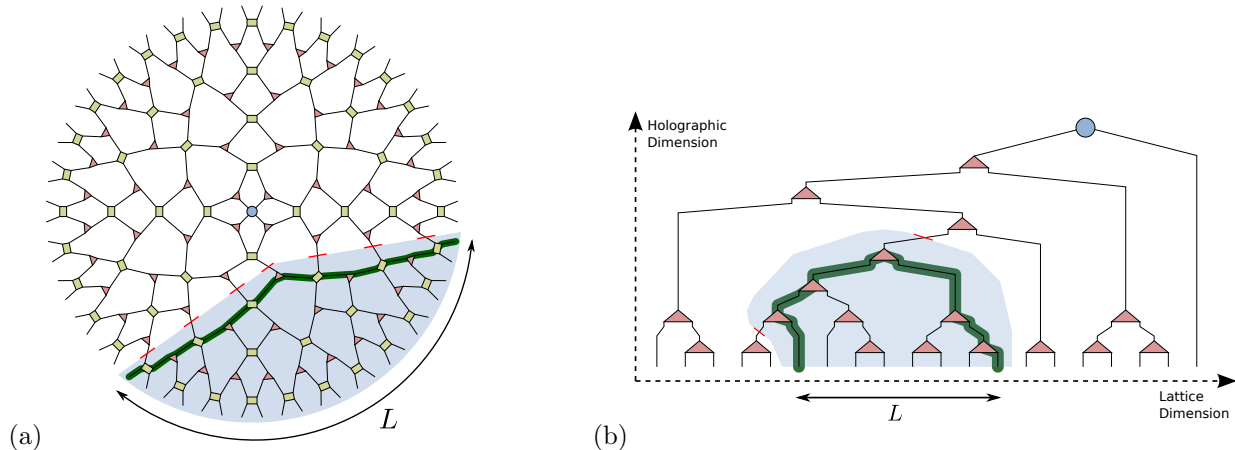
FIG. 4. (a) Tensor network diagram of a MERA with periodic boundary conditions where the green squares are *disentanglers*, pink triangles are *isometries* and the blue circle is the top tensor. A region of the network corresponding to L sites is highlighted in blue, where the bonds making up the minimum surface are highlighted by the red lines. The bold green line highlights a *geodesic* connecting two points on the lattice. (b) The SDRG algorithm as a TTN for a chain of $L = 20$ sites. Shapes and lines are as in (a). Lattice and holographic dimensions are indicated by the dashed arrows.

to the removal of local degrees of freedom in MERA and also suggests the possible usefulness of concepts from AdS/CFT for disordered spin chains.

The SDRG method was extended by Hikihara et. al. [30] to include higher states at each decimation, in the spirit of Wilson's numerical renormalisation group [31] and DMRG [15]. This method therefore decomposes the system into blocks rather than larger spins allowing for more accurate computation of, e.g., spin-spin correlation functions. The more states that are kept at each decimation the more accurate the description and it is exact in the limit of all states kept. This *numerical SDRG* amounts to a coarse-graining mechanism that acts on the operator. We show in reference [26] that it is equivalent to view this as a multi-level tensor network wavefunction acting on the original operator. The operators that coarse-grain two sites to one can be seen as *isometric tensors* or *isometries* that satisfy $ww^\dagger = \mathbb{1} \neq w^\dagger w$. When viewed in terms of isometries, the algorithm can self-assemble a tensor network based on the disorder of the system. When written in full, it builds an inhomogeneous binary tree tensor network (TTN) as shown in fig. 4(b). We shall henceforth refer to this TTN approach to SDRG as *tSDRG*. For a full description of the algorithm see reference [26].

A. Correlation Functions

The correlation functions for a strongly disordered Heisenberg chain are expected to disorder-average to a power-law decay with power $|x_2 - x_1|^{-2}$ [29]. As discussed in section III B, correlation functions in tensor networks scale as $e^{-\alpha D(x_1, x_2)}$, where $D(x_1, x_2)$ is the number of tensors that connect site x_1 to x_2 [16], for example $D(6, 13) = 5$ in fig. 4(b) highlighted in green. tSDRG has a holographic geometry based on a random TTN, with average path length $\langle D_{\text{TTN}} \rangle \approx \log |x_2 - x_1|$, i.e. scaling logarithmically with distance. This makes it ideally suited to capture the desired power law decay

$$\langle\langle \vec{s}_{x_1} \cdot \vec{s}_{x_2} \rangle\rangle \sim e^{-\alpha \langle D_{\text{TTN}}(x_1, x_2) \rangle} \sim e^{-\alpha \log |x_2 - x_1|} \sim |x_2 - x_1|^{-a}. \tag{11}$$
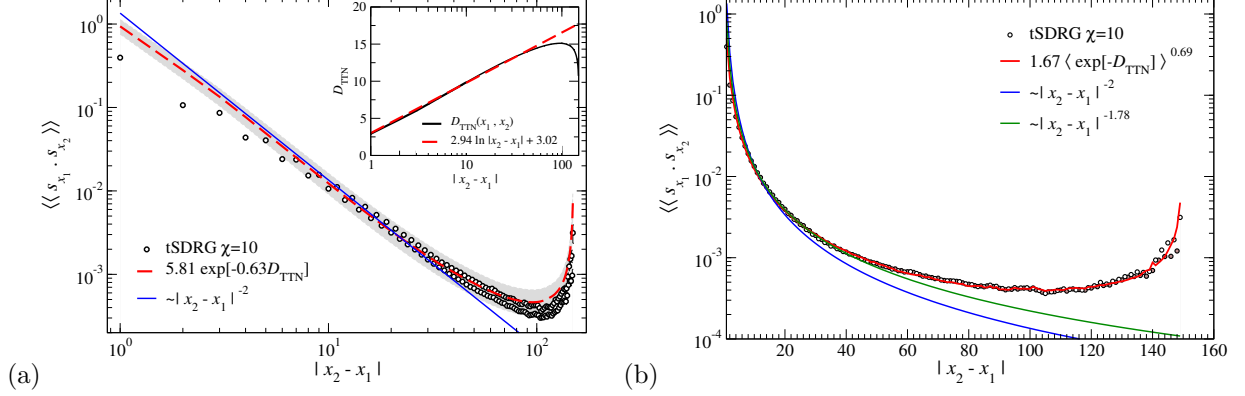
FIG. 5. (a) Reproduced from [26]. Correlation function for $L = 150$ averaged over 2000 samples for the direct calculation of $\langle\langle \vec{s}_{x_1} \cdot \vec{s}_{x_2}\rangle\rangle$ (black circles) and also via the holographic approach (11) using D_{TTN} (dashed red line with error of mean indicated by the grey shading) such that $\langle\langle \vec{s}_{x_1} \cdot \vec{s}_{x_2}\rangle\rangle \approx (5.81 \pm 0.93)\exp[-(0.62 \pm 0.02)D_{\mathrm{TTN}}]$. The expected thermodynamic scaling $|x_2 - x_1|^{-2}$ is also shown (solid blue line). Inset: The holographic path length D_{TTN} connecting sites x_1 and x_2 averaged over the 2000 TTNs (black) and a fit in the logarithmic regime (red). (b) Rescaled correlation function to remove odd-even effects on a semi-log plot. The expected thermodynamic scaling is shown as a solid blue line. The fitted scaling factor from (a) is plotted as a solid green line. The red line indicates the alternative holographic fitting with $\langle\langle \vec{s}_{x_1} \cdot \vec{s}_{x_2}\rangle\rangle \approx (1.67 \pm 0.10)\langle\exp[-D_{\mathrm{TTN}}]\rangle^{(0.69 \pm 0.01)}$.

In fig. 5(a), we show the behaviour of $\langle\langle \vec{s}_{x_1} \cdot \vec{s}_{x_2}\rangle\rangle$, with $\langle\langle \cdot \rangle\rangle$ denoting quantum and disorder averages, computed directly as well as its holographic estimate based on (11). We find that the behaviour for $|x_2 - x_1| \gg 1$ and $|x_2 - x_1| < L/2$ is indeed very similar for both approaches. We find that in the indicated distance regime, both measures of $\langle\langle \vec{s}_{x_1} \cdot \vec{s}_{x_2}\rangle\rangle$ are consistent with the expected r^{-2} behaviour. For $|x_2 - x_1| \gtrsim L/2$ we see that the boundaries lead to an upturn of $\langle\langle \vec{s}_{x_1} \cdot \vec{s}_{x_2}\rangle\rangle$ for both direct and holographic estimates. This upturn is a result of boundary effects and can easily be understood in terms of the holographic TNN; for $|x_2 - x_1| \geq L/2$, the average path length in the tree decreases [32]. In the inset of fig. 5(a) we show the distance dependence of D_{TTN} with $\chi = 10$. For $|x_2 - x_1| < L/2$, the data can be described by as linear behaviour in $\log|x_2 - x_1|$. We observe that as L increases, the resulting value of the scaling power a also increases towards the expected value of 2. We have also checked that the differences between $\chi = 10$ and 20 remain within the error bars and hence we use $\chi = 10$ for calculations of $\langle\langle \vec{s}_{x_1} \cdot \vec{s}_{x_2}\rangle\rangle$ in fig. 5(a). We further note that fig. 5(a) shows a clear difference in the correlation function between even and odd distances, due to the fact that singlets can only form with nearest neighbours on each coarse graining scale.

While eq. (11) neatly describes the power law behaviour of the data, a more accurate ansatz should be

$$\langle\langle \vec{s}_{x_1} \cdot \vec{s}_{x_2}\rangle\rangle \simeq A\langle e^{-D_{\mathrm{TTN}}(x_1,x_2)}\rangle^a. \tag{12}$$

We plot the fit to (12), along with the correlation data rescaled to remove the even-odd variation [33], in fig. 5(b). This shows that $\langle\langle \vec{s}_{x_1} \cdot \vec{s}_{x_2}\rangle\rangle \approx (1.67 \pm 0.10)\langle\exp[-D_{\mathrm{TTN}}]\rangle^{(0.69 \pm 0.01)}$ is a remarkably accurate fit to the data for all length scales. Our result implies that the majority of the correlation information is stored in the structure of the TTN rather than the contents of the tensors.

B. Entanglement Entropy

In general the entanglement entropy $S_{\mathrm{A|B}} = -\mathrm{Tr}\rho_{\mathrm{A}}\log_2\rho_{\mathrm{A}}$ is difficult to compute as the size of the reduced density matrix ρ_{A} scales exponentially with the size of block A. The TTN represen-
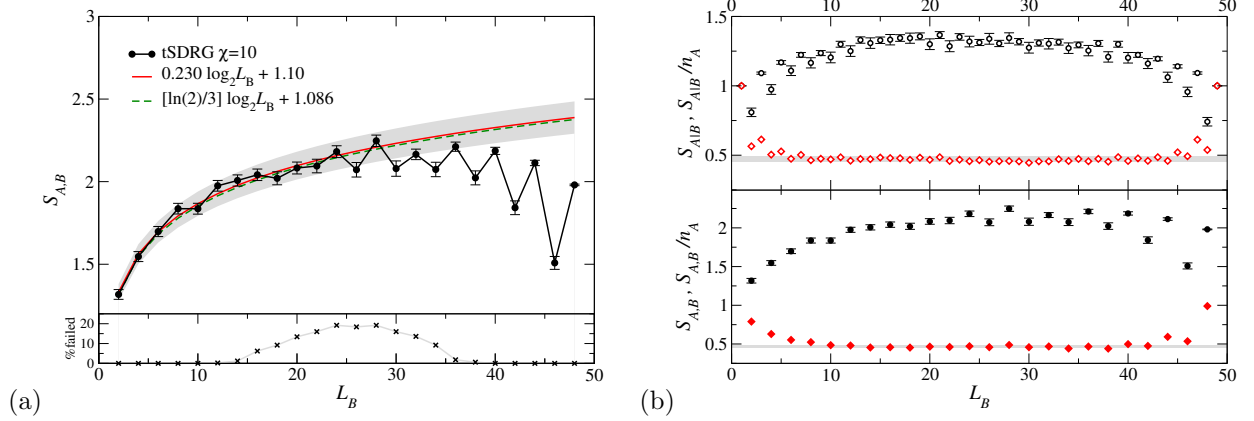
FIG. 6. Reproduced from [26]. (a) The entanglement entropy $S_{A,B}$ (black) averaged over 500 samples as a function of the size of a *block* L_B placed in the middle of a chain with $L = 50$ for $\chi = 10$. The fitting (red, solid line) gives $S_{A,B} = (0.22 \pm 0.02)\log_2 L_B + (1.12 \pm 0.05)$ for $L_B \leq 25$, above which finite size effects dominate. The grey shaded region indicates the accuracy of the fit. The (green) dashed line shows the entanglement scaling from ref. [34] with the vertical position fitted to the point $L_B = 2$. The straight black lines are a guide to the eye only. At the bottom, we show the failure rate in percent (crosses) for different L_B. (b) Entanglement entropy S (black circles) and entanglement entropy per bond S/n_A (red diamonds) for left-right bipartitions A|B (top, open symbols) and central blocks A, B (bottom, filled symbols) with $\chi = 10$. The entanglement per bond saturates to 0.47 ± 0.02 for bipartitions and 0.48 ± 0.02 for blocks (grey shaded regions).

tation of tSDRG gives an alternative means of finding $S_{A|B}$ for any bipartitions A and B of the system. In a similar manner to the correlation functions, the geometry of the tensor network is related to its ability to capture entanglement. As discussed in section III B, $S_{A|B}$ is proportional to the minimum number of indices, n_A, that one would have to cut to separate a block A of spins from the rest B of the chain [16, 26]. For the TTN the position of the block in the chain alters the number of indices that have to be cut to separate it from the rest of the system. This suggests that there are spatial regions in the chain that are more and less entangled, which is likely to be true for a strongly disordered spin chain.

In refs. [34, 35], Refael and Moore calculate a *block* entanglement $S_{A,B}$ in the random singlet phase and show that it scales as $(\ln[2]/3)\log_2 L_B$ where region B is a block of extent L_B in the centre of the spin chain. We show the resulting $S_{A,B}$ in fig. 6(a). The figure clearly indicates that finite size effects become prevalent for large L_B, so we fit for $L_B \leq L/2$ only. The resulting scaling behaviour $S_{A,B} \approx (0.22 \pm 0.02)\log_2 L_B$ is fully consistent with previous results [35]. We also examine the entanglement entropy per bond, S/n_A, of a TTN for both left-right bipartitions A|B and blocks A, B with $\chi = 10$ when averaging over 500 disorder configurations with $L = 50$. Figure 6(b) shows that away from the boundaries S/n_A saturates to the same constant 0.47 ± 0.02 in both cases. Note that for $L_B \sim L/2$, we find that up to 20% of our samples for $\chi = 10$ lead to calculations of $S_{A,B}$ consuming memory beyond 100GB and therefore fail to complete. Nevertheless, we believe that this will not greatly change the average values of $S_{A,B}/n_A$ reported here as the higher failure rate is for block sizes where boundary conditions become influential, which is supported by the calculations for smaller χ. For $\chi = 4$ we find 0.42 ± 0.02 for both blocks and bipartitions with a much lower failure rate ($< 1\%$) due to the smaller size of the density matrices. This might conceivably suggest that $S/n_A = 0.5$ is a limiting value for larger χ and L. This is consistent with ref. [16] and implies that the entanglement entropy is proportional to the length of the holographic minimal surface that connects the two blocks.

V.   CONCLUSIONS AND OUTLOOK

The use of tensor networks within the fields of condensed matter physics and quantum information theory is becoming ever more common. MPS based DMRG is widely believed to be the most accurate method of numerically modelling 1D systems and it is being applied in increasingly complicated scenarios [4, 5]. PEPS are being used both as a numerical method and as an analytic platform to study two dimensional strongly correlated systems, particularly topological phases of matter [36, 37]. MERA and holographic tensor networks are beginning to be applied in various other fields such as in high energy physics to potentially link entanglement and gravity [38], and quantum information in the creation of holographic error correction codes [39].

There are many ways that tensor networks can aid the study of disordered systems. Although DMRG is in some ways imperfect for the modelling of disorder, it is so efficient that much can still be learned by applying it [40]. Beyond the Heisenberg and Bose-Hubbard models, there are still a myriad of possible Hamiltonians that can be examined with DMRG. A current area of intense research is many-body localisation (MBL), the generalisation of Anderson localisation to interacting many-body systems [41]. It is believed that the area law holds for all excited states in systems with MBL up to some mobility energy, unlike gapped quantum systems where only the ground state is area law satisfying [42]. This in principle should allow for an efficient MPS representation, and therefore accurate DMRG simulation, of any state in a 1D MBL spectrum. Strong disorder renormalisation techniques such as tSDRG can be used as high precision methods when disorder is strong. The method should be accurate for use with the FM/AFM disordered spin-1/2 Heisenberg model where large effective spins would be created as the renormalisation progresses [30]. Beyond spin-1/2 there have been exciting discoveries in disordered spin-3/2 Heisenberg systems, where the rich phase diagram contains topological phases as well as spin doublet and triplet phases [43]. It would be fascinating to uncover the optimal tensor network geometries in these situations.

More generally our results suggest that it might be possible to construct an algorithm that can decide autonomously on the best network geometry for a particular system under consideration. Currently the geometry in most tensor network approaches is set by hand using prior knowledge of the model. In a network that can self optimise the structure, the final geometry can become a resource for learning about the properties of the wavefunction. Perhaps with these ideas, truly scalable 2D and 3D tensor network algorithms may emerge for clean and disordered systems.

---

[1]   M. Srednicki, Phys. Rev. Lett. **71**, 666 (1993).
[2]   M. B. Hastings, J. Stat. Mech. Theor. Exp. **2007**, P08024 (2007).
[3]   J. Eisert, M. Cramer, and M. B. Plenio, Rev. Mod. Phys. **82**, 277 (2010).
[4]   R. Orús, Ann. Phys. **349**, 117 (2014).
[5]   U. Schollwöck, Ann. Phys. **326**, 96 (2011).
[6]   J. Bekenstein, Lett. Nuovo Cimento Series 2 **4**, 737 (1972).
[7]   S. W. Hawking, Nature **248**, 30 (1974).
[8]   S. Ryu and T. Takayanagi, Phys. Rev. Lett. **96**, 181602 (2006).
[9]   J. Maldacena, Int. J. Theor. Phys. **38**, 1113 (1999).
[10]   J. McGreevy, Adv. High Energy Phys. **2010**, 723105 (2010).
[11]   I. Peschel and V. Eisler, in *Computational Many-Particle Physics*, Vol. 739 of *Lect. Notes Phys.*, edited by H. Fehske, R. Schneider, and A. Weiße (Springer, Berlin, Heidelberg, 2008), pp. 581–596.
[12]   G. M. Crosswhite and D. Bacon, Phys. Rev. A **78**, 012356 (2008).
[13]   N. Laflorencie and D. Poilblanc, in *Quantum Magnetism*, edited by U. Schollwöck, J. Richter, D. J. J. Farnell, and R. F. Bishop (Springer, Berlin, Heidelberg, 2004), pp. 227–252.
[14]   K. A. Hallberg, Adv. Phys. **55**, 477 (2006).

[15] S. R. White, Phys. Rev. Lett. **69**, 2863 (1992).
[16] G. Evenbly and G. Vidal, J. Stat. Phys. **145**, 891 (2011).
[17] G. Vidal, J. I. Latorre, E. Rico, and A. Kitaev, Phys. Rev. Lett. **90**, 227902 (2003).
[18] J. I. Latorre, E. Rico, and G. Vidal, Quantum Info. Comput. **4**, 48 (2004).
[19] F. Verstraete and J. I. Cirac, arXiv:cond-mat/0407066v1 (2004).
[20] F. Verstraete, V. Murg, and J. I. Cirac, Adv. Phys. **57**, 143 (2008).
[21] G. Vidal, Phys. Rev. Lett. **99**, 220405 (2007).
[22] G. Evenbly and G. Vidal, Phys. Rev. B **79**, 144108 (2009).
[23] B. Swingle, Phys. Rev. D **86**, 065007 (2012).
[24] M. Nozaki, S. Ryu, and T. Takayanagi, J. High Energy Phys. **2012**, 193 (2012).
[25] A. Mollabashi, M. Nozaki, S. Ryu, and T. Takayanagi, J. High Energy Phys. **2014**, 1 (2014).
[26] A. M. Goldsborough and R. A. Römer, Phys. Rev. B **89**, 214203 (2014).
[27] S.-k. Ma, C. Dasgupta, and C.-k. Hu, Phys. Rev. Lett. **43**, 1434 (1979).
[28] C. Dasgupta and S.-k. Ma, Phys. Rev. B **22**, 1305 (1980).
[29] D. S. Fisher, Phys. Rev. B **50**, 3799 (1994).
[30] T. Hikihara, A. Furusaki, and M. Sigrist, Phys. Rev. B **60**, 12116 (1999).
[31] K. G. Wilson, Rev. Mod. Phys **47**, 773 (1975).
[32] A. M. Goldsborough *et al.*, arXiv:1502.07893 [math-ph] (2015).
[33] J. A. Hoyos, A. P. Vieira, N. Laflorencie, and E. Miranda, Phys. Rev. B **76**, 174425 (2007).
[34] G. Refael and J. E. Moore, Phys. Rev. B **76**, 024419 (2007).
[35] G. Refael and J. E. Moore, Phys. Rev. Lett. **93**, 260602 (2004).
[36] T. B. Wahl, H.-H. Tu, N. Schuch, and J. I. Cirac, Phys. Rev. Lett. **111**, 236805 (2013).
[37] D. Poilblanc, J. I. Cirac, and N. Schuch, Phys. Rev. B **91**, 224431 (2015).
[38] B. Swingle and M. V. Raamsdonk, arXiv:1405.2933 [hep-th] (2014).
[39] F. Pastawski, B. Yoshida, D. Harlow, and J. Preskill, J. High Energy Phys. **2015**, 1 (2015).
[40] A. M. Goldsborough and R. A. Römer, EPL **111**, 26004 (2015).
[41] D. Basko, I. Aleiner, and B. Altshuler, Ann. Phys. **321**, 1126 (2006).
[42] A. Chandran *et al.*, Phys. Rev. B **92**, 024201 (2015).
[43] V. L. Quito, J. A. Hoyos, and E. Miranda, Phys. Rev. Lett. **115**, 167201 (2015).